Journal of Computational Physics **158,** 1–27 (2000)
doi:10.1006/jcph.1999.6400, available online at http://www.idealibrary.com on IDEAL®

Development of an Improved Gas-Kinetic BGK Scheme for Inviscid and Viscous Flows

Dongsuk Chae, Chongam Kim, and Oh-Hyun Rho

Department of Aerospace Engineering, Seoul National University, Seoul 151-742, Korea

Received May 10, 1999; revised October 11, 1999

This paper deals with the development of an improved gas-kinetic BGK scheme for inviscid and viscous flow fields. As the first step toward efficient calculation, particle distribution functions in the general solution of the BGK model are simplified to the extent that the essential features of the standard gas-kinetic BGK scheme are not lost. Then, improved schemes are suggested, which overcome difficulties that may arise in the applications of BGK-type schemes to compressible viscous flow calculations. A Prandtl number correction method is also developed to allow the present schemes to work for arbitrary Pr number. For steady state problems, convergence acceleration techniques suitable for the present schemes are developed in the framework of an implicit time integration. Various numerical experiments ranging from one-dimensional shock tubes to viscous turbulent flows are performed to demonstrate accuracy, robustness, and other essential features of the present method.

Key Words: gas-kinetic BGK scheme; convergence acceleration; Pr number correction; viscous turbulent flows.

1. INTRODUCTION

Many numerical schemes have been developed to predict compressible inviscid and viscous flows using the abilities of fast computing machines. Designing efficient numerical schemes possessing a high degree of accuracy and robustness is the central issue in this field. Although great advances have been achieved toward this goal, none of them seems to be perfect enough to pass all the numerical tests set by many researchers. Most notable and successful among them are Godunov-type schemes and flux vector splitting schemes, in which the wave interactions of the Euler equations are resolved in an upwind manner. As those numerical methods are applied to various aerodynamic problems of speeds ranging from subsonic to hypersonic, some serious drawbacks have surfaced. The flux vector splitting schemes usually provide efficient and robust results even in very severe environments involving strong shocks and vacuum-like flows. However, the ignorance of

0021-9991/00 $35.00

contact discontinuities precludes the accurate calculation of viscous flows, which is hardly alleviated by higher order spatial interpolation or mesh refinement near a wall. In the family of Godunov-type schemes, Roe's FDS (Flux Difference Splitting) scheme [1] has enjoyed great popularity owing to its accuracy for both compressible inviscid and viscous flows. This method, by introducing the average state flux Jacobian satisfying the Rankine–Hugoniot relation, solves exactly the locally linearized Euler equations and can capture a shock within one computational cell. It was not until Quirk's extensive catalogue [2] on the pathological behaviors of Roe's scheme that issues regarding the robustness of numerical schemes drew much attention. The transverse shock instability and negative internal energy of Godunov-type schemes are reported to be the main threats to the computation of high speed flows with strong shock waves and expansion fans. Remedies for such spurious behaviors generally lie in modifying wave speeds at the expense of accuracy. Thus, contemporary concern for the development of numerical schemes is mainly directed toward combining the accuracy of Godunov-type schemes and the robustness of flux vector splitting schemes.

Besides the numerical schemes stemming from the discretization of the Euler equations, several gas-kinetic schemes have been developed based on the Boltzmann equation. Pullin was the first one who developed a finite-volume upwind flux for the Euler equations, called the EFM (Equilibrium Flux Method) [3]. Reitz also developed a numerical scheme based on the numerical integration of the Maxwellian distribution [4]. Perthame [5] and Mandal and Desphande [6] further explored the EFM approach rigorously to derive some useful properties about positivity and entropy conditions. Since these methods, however, allow particles to penetrate a cell interface without collisions during unit computational time, they usually produce a large numerical viscosity and heat conduction, whose merits and demerits are shared with the flux vector splitting schemes from the Euler equations [7]. As a way to reduce the numerical dissipation of these methods, Macrossan and Oliver proposed the EIM (Equilibrium Interface Method), where particle collisions are introduced instantaneously in computing a numerical flux at a cell interface [8]. A similar approach with a different name, the TTT (Totally Thermalized Transport) scheme [9] was also proposed independently by Xu. These methods can resolve a shock layer or a boundary layer accurately, but they may yield numerical oscillations in capturing rarefaction waves. More recently, Moschetta and Pullin proposed a hybrid solver (EFMO) which augments the EFM with Osher's approximate Riemann solver for the accurate capturing of contact discontinuity [10].

One of the distinct approaches to take particle collision effect into consideration in gas evolution stage can be found in Xu and Prendergast [11, 12] and Xu *et al.* [13]. In this method, the collision effect is considered by the BGK model as an approximation of the collision integral in the Boltzmann equation. It is found that this gas-kinetic BGK scheme has accuracy superior to flux vector splitting schemes and avoids the anomalies of Godunov-type schemes. The other desirable characteristics of BGK-type schemes are also discussed in Refs. [11–13].

The gas-kinetic BGK scheme, however, is not completely free from shortcomings in the computation of steady inviscid and viscous flows. In the present paper, we notice several difficulties of the BGK-based scheme which may arise in the computation of compressible viscous flows and eliminate them by modifying one of its flux components. During this process, the relation between the BGK numerical flux and other kinetic fluxes such as the EFM, EIM, or TTT schemes is clarified. Also, an efficient method of Prandtl number correction is proposed for the proper calculation of thermal conduction effects. In order

to get a sufficiently converged steady state solution, implicit formulation and a local time stepping consistent with the BGK-based scheme are proposed. For efficient steady state calculations, a multigrid method suitable for the proposed schemes is also developed.

This paper is organized as follows. In Section 2, the construction of the standard gas-kinetic BGK scheme is presented. Referring to a few issues of the derived scheme in compressible viscous calculations, modified gas-kinetic BGK schemes with a Prandtl number correction are proposed. In addition, temporal discretization and convergence acceleration techniques are dealt with. In Section 3, we apply the schemes developed in Section 2 to various numerical tests in order to demonstrate their essential features. Finally, concluding remarks are made.

2. NUMERICAL METHODS

2.1. *Standard Gas-Kinetic BGK Scheme*

A standard gas-kinetic BGK scheme [11] [12] begins with the Boltzmann equation and it is written in two dimensions as

$$\frac{\partial f}{\partial t} + u\frac{\partial f}{\partial x} + v\frac{\partial f}{\partial y} = \frac{\delta f}{\delta t}, \tag{1}$$

where f is a particle distribution function and the right hand side stands for a collision term. Bhatnagar *et al.* [14] suggested a relaxation model as an approximation of the complicated collision term in Eq. (1), which can be written as

$$\frac{\partial f}{\partial t} + u\frac{\partial f}{\partial x} + v\frac{\partial f}{\partial y} = \frac{g - f}{\tau}, \tag{2}$$

where f is a real particle distribution function and g is an equilibrium particle distribution function which f approaches through particle collisions within a collision time scale τ. Both f and g are functions of space (x, y), time (t), particle velocity (u, v), and ξ. ξ is the K-dimensional vector of internal velocities introduced to conveniently describe the internal energy and specific heats for a perfect gas. The internal degree of freedom K is connected to the space dimension and the ratio of specific heats by the relation $K + D = 2/(\gamma - 1)$. If the particle distribution function f is known, under the assumption of hydrodynamic limit, macroscopic variables such as mass density $\rho(x, y, t)$, momentum density $\mathbf{P}(x, y, t)$, and total energy density $\varepsilon(x, y, t)$ are obtained from the moment relation as

$$\begin{pmatrix} \rho \\ P_x \\ P_y \\ \varepsilon \end{pmatrix} = \int f \Psi \, d\Xi, \tag{3}$$

where $d\Xi = \xi^{K-1}\, d\xi\, du\, dv$ is an infinitesimal volume element in phase space and Ψ is the vector of the following form:

$$\Psi = \left[1, u, v, \frac{1}{2}(u^2 + v^2 + \xi^2)\right]^{\mathrm{T}}. \tag{4}$$

With the moment relation described in Eq. (3), a physical flux in the x-direction through a

cell interface during time step Δt can be expressed as

$$\mathbf{F}_x = \int_0^{\Delta t} \int u f \Psi \, d\Xi \, dt. \tag{5}$$

A general solution f of Eq. (2) at the cell interface $(x_{i+1/2}, y_j)$ is obtained as

$$f(x, y, t, u, v, \xi) = \frac{1}{\tau} \int_0^t g(x', y', t, u, v, \xi) e^{-(t-t')/\tau} \, dt' + e^{-t/\tau} f_0(x - ut, y - vt), \tag{6}$$

where $x' = x_{i+1/2} - u(t - t')$ and $y' = y_j - v(t - t')$ are particle trajectories and f_0 is the initial non-equilibrium distribution function at $t = 0$. The development of the present numerical flux essentially lies in the reasonable construction of the distribution function f in Eq. (6) conforming to the underlying physics. A proper discretization of two distribution functions g and f_0 was originally proposed by Xu *et al.* [11] as the form

$$f_0 = \begin{cases} g^l(1 + a^l x + b^l y), & x < 0 \\ g^r(1 + a^r x + b^r y), & x > 0 \end{cases}, \tag{7a}$$

$$g = g_0(1 + \bar{a}x + \bar{b}y + \bar{A}t), \tag{7b}$$

where g^l, g^r, and g_0 are local Maxwellian distributions at the left, right, and middle of a cell interface, respectively. The distribution function g is the Taylor series expansion to the first order of time and space near the middle of the cell interface. Spatial slopes $\bar{a}$ and $\bar{b}$ have the following dependency on u, v, and ξ:

$$\bar{a} = a_1 + a_2 u + a_3 v + a_4(u^2 + v^2 + \xi^2), \tag{8a}$$

$$\bar{b} = b_1 + b_2 u + b_3 v + b_4(u^2 + v^2 + \xi^2), \tag{8b}$$

where all the coefficients a_{1-4}, b_{1-4} are considered to be locally constant. The spatial slopes a^l, a^r, b^l, and b^r in the function f_0 have the similar properties. The determination of these coefficients will be discussed later. Since the gas-kinetic BGK scheme allows us the flexible construction of the two functions, the following forms different from Eqs. (7a), (7b) are suggested:

$$f_0 = \begin{cases} g^l, & x < 0 \\ g^r, & x > 0 \end{cases}, \tag{9a}$$

$$g = g_0(1 + \bar{a}x + \bar{b}y). \tag{9b}$$

The spatial slope terms in f_0 are discarded to reduce the computational cost and unnecessary numerical dissipation since they appear as additional diffusive fluxes in the final numerical flux form, which is undesirable for the design of a BGK-based scheme for viscous flows. The temporal slope term $\bar{A}$ in g which couples the spatial slopes with the temporal one to yield the second order temporal accuracy [13, 15] is also neglected in the present approach for the improvement of convergence characteristics and computational efficiency. Due to its time evolutionary character, $\bar{A}$ is particularly suitable for unsteady flow computations but it shows a very slow convergence behavior in steady state calculations, which can be usually observed in Lax–Wendroff type schemes [13, 15]. Detailed analysis and computed results will be given later.

Using the relation between the gas distribution function and the macroscopic variables in Eq. (3), we get

$$\int g^* \Psi \, d\Xi = \begin{pmatrix} \rho^* \\ P_x^* \\ P_y^* \\ \varepsilon^* \end{pmatrix}, \tag{10}$$

where the superscript * denotes the left or right state variables at the cell interface $(x_{i+1/2}, y_j)$. The Maxwellian g^* is then given by

$$g^* = \rho^* \left(\frac{\lambda^*}{\pi}\right)^{(K+2)/2} e^{-\lambda^*[(u-U^*)^2+(v-V^*)^2+\xi^2]}, \tag{11}$$

where the parameters ρ^*, U^*, V^*, and $\lambda^*(=(2RT^*)^{-1}$ with gas constant R and temperature T^*) can be uniquely determined from Eq. (10) as

$$\begin{pmatrix} \rho^* \\ U^* \\ V^* \\ \lambda^* \end{pmatrix} = \begin{pmatrix} \rho^* \\ P_x^*/\rho^* \\ P_y^*/\rho^* \\ \frac{(K+2)\rho^*}{4(\varepsilon^* - 1/2(P_x^{*2}+P_y^{*2})/\rho^*)} \end{pmatrix}. \tag{12}$$

Flow variables on the right hand side of Eq. (12) are obtained from the MUSCL [16] interpolation for a higher order spatial accuracy as

$$\begin{aligned} Q_l = Q_{i,j} + \frac{s}{4}\Bigg\{ & (1-k)\phi\left(\frac{\Delta Q_{i+1/2,j}}{\Delta Q_{i-1/2,j}}\right)\Delta Q_{i-1/2,j} \\ & + (1+k)\phi\left(\frac{\Delta Q_{i-1/2,j}}{\Delta Q_{i+1/2,j}}\right)\Delta Q_{i+1/2,j}\Bigg\}, \end{aligned} \tag{13a}$$

$$\begin{aligned} Q_r = Q_{i+1,j} - \frac{s}{4}\Bigg\{ & (1-k)\phi\left(\frac{\Delta Q_{i+1/2,j}}{\Delta Q_{i+3/2,j}}\right)\Delta Q_{i+3/2,j} \\ & + (1+k)\phi\left(\frac{\Delta Q_{i+3/2,j}}{\Delta Q_{i+1/2,j}}\right)\Delta Q_{i+1/2,j}\Bigg\}, \end{aligned} \tag{13b}$$

where Q is a conservative variable and $\Delta Q_{i+1/2,j} = Q_{i+1,j} - Q_{i,j}$. ϕ is a limiter function preventing spurious oscillations in the vicinity of physical discontinuities. Van Leer's limiter of the form $\phi(r) = (r + |r|)/(1 + r)$ is employed for all the calculations performed in this paper. The value of $s = 1$ and $k = -1$ is used to obtain the second order spatial accuracy. On the other hand, the parameters of the Maxwellian g_0 can be determined from the conservation constraint as

$$\int (g - f)\Psi \, d\Xi = 0 \qquad \text{for all } (x, y) \text{ and } t. \tag{14}$$

Since we can locate the cell interface at $(x_{i+1/2}, y_j) = (0, 0)$ without loss of generality, the

conservation constraint at $t = 0$, substituting Eqs. (9a), (9b) into Eq. (14), is expressed as

$$\begin{pmatrix} \rho_0 \\ P_{0x} \\ P_{0y} \\ \varepsilon_0 \end{pmatrix} = \begin{pmatrix} \rho^l \langle u^0 \rangle^+ + \rho^r \langle u^0 \rangle^- \\ \rho^l \langle u^1 \rangle^+ + \rho^r \langle u^1 \rangle^- \\ \rho^l \langle v^1 \rangle^+ + \rho^r \langle v^1 \rangle^- \\ \rho^l \langle u^2 + v^2 + \xi^2 \rangle^+ + \rho^r \langle u^2 + v^2 + \xi^2 \rangle^- \end{pmatrix}, \tag{15}$$

where the following notations are introduced:

$$\langle Q^n \rangle^+ = \frac{1}{\rho^l} \int_0^\infty Q^n g^l \, d\Xi, \qquad \langle Q^n \rangle^- = \frac{1}{\rho^r} \int_{-\infty}^0 Q^n g^r \, d\Xi. \tag{16}$$

The quantities with subscript 0 at the cell interface in Eq. (15) are identical to the equilibrium state proposed to calculate the numerical fluxes in EIM or TTT scheme. With the known variables ρ_0, P_{0x}, P_{0y}, and ε_0 from Eq. (15), Eq. (12) is used to give the parameters of the Maxwellian g_0, or ρ_0, U_0, V_0 and λ_0. All the moment calculations involved in the integration of the Maxwellian in phase space from negative infinity to zero or zero to positive infinity can be expressed by exponential and error functions. Higher order moments are easily calculated by recurrence formulas through integration by parts as in Ref. [15]. The spatial slope $\bar{a}$ in g at $(x_{i+1/2}, y_j) = (0, 0)$ is calculated from the relation

$$\int g_0 \bar{a} \Psi \, d\Xi = \frac{1}{\Delta x} \begin{pmatrix} \rho_{i+1,j} - \rho_{i,j} \\ P_{x_{i+1,j}} - P_{x_{i,j}} \\ P_{y_{i+1,j}} - P_{y_{i,j}} \\ \varepsilon_{i+1,j} - \varepsilon_{i,j} \end{pmatrix}, \tag{17}$$

where Δx is a distance between the centers of two neighboring cells. Equation (17), after integration on the left hand side, can be expressed as

$$\begin{pmatrix} 1 & U_0 & V_0 & M_1 \\ U_0 & U_0^2 + \frac{1}{2\lambda_0} & U_0 V_0 & M_2 \\ V_0 & U_0 V_0 & V_0^2 + \frac{1}{2\lambda_0} & M_3 \\ M_1 & M_2 & M_3 & M_4 \end{pmatrix} \begin{pmatrix} a_1 \\ a_2 \\ a_3 \\ a_4 \end{pmatrix} = \frac{1}{\Delta x} \begin{pmatrix} \rho_{i+1,j} - \rho_{i,j} \\ P_{x_{i+1,j}} - P_{x_{i,j}} \\ P_{y_{i+1,j}} - P_{y_{i,j}} \\ \varepsilon_{i+1,j} - \varepsilon_{i,j} \end{pmatrix}, \tag{18}$$

where

$$M_1 = \frac{1}{2}\left(U_0^2 + V_0^2 + \frac{K+2}{2\lambda_0} \right), \qquad M_2 = \frac{1}{2}\left(U_0^3 + U_0 V_0^2 + \frac{(K+4)U_0}{2\lambda_0} \right),$$
$$M_3 = \frac{1}{2}\left(U_0^3 + U_0^2 V_0 + \frac{(K+4)V_0}{2\lambda_0} \right),$$
$$M_4 = \frac{1}{2}\left[\left(U_0^2 + V_0^2 \right)^2 + \frac{(K+4)\left(U_0^2 + V_0^2 \right)}{\lambda_0} + \frac{(K^2 + 6K + 8)}{4\lambda_0^2} \right].$$

Note that the 4×4 matrix in Eq. (18) is symmetric and can be efficiently inverted to determine the spatial slope coefficients. The coefficients related to the y-directional spatial slope $\bar{b}$ can be obtained in a similar fashion. Since all the parameters and the coefficients of spatial

slopes have been determined up to this point, the general solution at $(x_{i+1/2}, y_j) = (0, 0)$ in Eq. (6), after substituting Eqs. (9a) and (9b), is written as

$$f(0,0,t,u,v,\xi) = \left(1 - e^{-t/\tau}\right) g_0 + e^{-t/\tau} f_0(-ut, -vt) + \left(\tau\left(-1 + e^{-t/\tau}\right) + te^{-t/\tau}\right)(u\bar{a} + v\bar{b})g_0, \tag{19}$$

which is used to give the time-averaged gas-kinetic BGK numerical flux at the cell interface in the x-direction as

$$\mathbf{F}_x(\mathbf{Q}_l, \mathbf{Q}_r, \tau, \Delta t) = \frac{1}{\Delta t}\int_0^{\Delta t}\int u f(0,0,t,u,v,\xi)\Psi \, d\Xi \, dt, \tag{20}$$

where Δt is a computational time step. The numerical flux in the y-direction can be calculated similarly after an appropriate coordinate transformation.

The only unknown variable left in the numerical flux formula of Eq. (20) is the particle collision time, which plays an important role in the accuracy and robustness of the present scheme. The collision time can be directly obtained from the relation between collision time, pressure, and viscosity as

$$\tau p = \mu. \tag{21}$$

After non-dimensionalizing τ, p, ρ, and μ by free stream values L/a_∞, $\rho_\infty a_\infty^2$, ρ_∞ and μ_∞, respectively, the collision time can be expressed by

$$\hat{\tau} = \frac{M_\infty \hat{\mu}}{\mathrm{Re}_\infty \hat{p}}, \tag{22}$$

where a hat denotes non-dimensionalized variables. M_∞ and Re_∞ are the Mach number and Reynolds number based on free stream quantities, and a_∞ is the free stream speed of sound. The viscosity is calculated from the Sutherland's law given by

$$\hat{\mu} = \frac{\mu}{\mu_\infty} = \left(\frac{T}{T_\infty}\right)^{3/2}\frac{T_\infty + S}{T + S}, \tag{23}$$

where $S = 110.4$ K and $T_\infty = 285$ K. The pressure $\hat{p}$ is the equilibrium interface pressure obtained by $\hat{\rho}_0/(2\hat{\lambda}_0)$. Since the shock thickness is the order of the mean free path of molecules in continuum gas dynamics, another collision term which plays the role of numerical dissipation is necessary in order to capture shock discontinuities without unphysical oscillations within finite computational cells. Thus the collision time has the form

$$\hat{\tau} = \frac{M_\infty \hat{\mu}}{\mathrm{Re}_\infty \hat{p}} + C_2 \frac{\sqrt{\hat{\lambda}_0}}{\hat{\rho}_0}|\hat{p}^l - \hat{p}^r|, \tag{24}$$

where the coefficient C_2 can be empirically determined. For inviscid calculations, the physical part of the collision time is given by $\tau = l/\bar{v}$ from gas-kinetic theory. The mean free path, l, can be written as the function of local number density n and a molecular cross section σ as $l \propto 1/n\sigma$, and the mean thermal speed of molecules $\bar{v}$ is proportional to the square root of temperature. Hence, the collision time for inviscid flows can be expressed as

$$\hat{\tau} = C_1 \frac{\sqrt{\hat{\lambda}_0}}{\hat{\rho}_0} + C_2 \frac{\sqrt{\hat{\lambda}_0}}{\hat{\rho}_0}|\hat{p}^l - \hat{p}^r|. \tag{25}$$

In this case, both the first and the second part of the collision time is treated purely for a numerical purpose. The first part is the numerical dissipation in smooth regions while the second part is to capture shock discontinuities. The coefficient C_1 is also empirically determined. The value of C_1 is fixed as 5×10^{-5} in all numerical calculations performed in this paper, and C_2 is 1×10^{-4} except for the cases denoted specifically. Solution accuracy, however, is not so sensitive to the variation of C_2, as will be demonstrated in later section. However, we still believe that the present choice of the collision time is not optimal, and further research on this subject is necessary.

The numerical flux of the present method at the cell interface, after Eq. (19) is substituted into Eq. (20), takes the form

$$\begin{aligned}\mathbf{F}_{i+1/2,j} = &\left(1-\tau\left(1-e^{-\Delta t/\tau}\right)/\Delta t\right)\mathbf{F}^{\mathrm{I}} + \tau\left(1-e^{-\Delta t/\tau}\right)/\Delta t\mathbf{F}^{\mathrm{II}} + \tau\left((2\tau-\Delta t)\right.\\ &\left.-(\Delta t+2\tau)e^{-\Delta t/\tau}\right)/\Delta t\mathbf{F}^{\mathrm{III}},\end{aligned} \tag{26}$$

where

$$\mathbf{F}^{\mathrm{I}} = \mathbf{F}^{\mathrm{EIM}\,or\,\mathrm{TTT}} = \begin{pmatrix} \rho_0 U_0 \\ \rho_0\left(U_0^2 + 1/(2\lambda_0)\right) \\ \rho_0 U_0 V_0 \\ \rho_0\left(U_0^3 + U_0 V_0^2 + 2U_0/\lambda_0 + K(K+2)U_0/\left(4\lambda_0^2\right)\right) = \rho_0 U_0 H_0 \end{pmatrix}, \tag{27}$$

$$\begin{aligned}\mathbf{F}^{II} = \mathbf{F}^{\mathrm{EFM}} = \mathbf{F}_l^+ + \mathbf{F}_r^- = &\begin{pmatrix} M_l^+ \rho_l a_l \\ M_l^+ \rho_l a_l U_l + P_l^+ \rho_l/(2\lambda_l) \\ M_l^+ \rho_l a_l V_l \\ M_l^+ \rho_l a_l H_l - \frac{\rho_l a_l}{8\alpha\lambda_l\sqrt{\pi}}\exp\left(-\alpha^2 M_l^2\right) \end{pmatrix} \\ &+ \begin{pmatrix} M_r^- \rho_r a_r \\ M_r^- \rho_r a_r U_r + P_r^- \rho_r/(2\lambda_r) \\ M_r^+ \rho_r a_r V_r \\ M_r^- \rho_r a_r H_r + \frac{\rho_r a_r}{8\alpha\lambda_r\sqrt{\pi}}\exp\left(-\alpha^2 M_r^2\right) \end{pmatrix},\end{aligned} \tag{28}$$

and

$$\mathbf{F}^{\mathrm{III}} = \int u(u\bar{a} + v\bar{b}) g_0 \Psi \, d\Xi. \tag{29}$$

Here, $M^{\pm} = \pm\frac{\exp(-\alpha^2 M^2)}{2\alpha\sqrt{\pi}} + M\frac{\mathrm{erfc}(\mp\alpha M)}{2}$, $P^{\pm} = \frac{\mathrm{erfc}(\mp\alpha M)}{2}$, and $\alpha = \sqrt{\gamma/2}$. For a general two-dimensional mesh, M is the Mach number normal to the cell interface, and (U_*, V_*) are the velocity components in the direction normal and tangential to the cell interface. a is the speed of sound and H is the total enthalpy. The explicit form of $\mathbf{F}^{\mathrm{III}}$ is described in Appendix. It can be observed from Eq. (26) that the present flux, through the non-linear coupling by the particle collision time, is composed of the contributions from three fluxes. The numerical flux $\mathbf{F}^{\mathrm{I}}$ is the EIM [8] or TTT [9] flux whose numerical dissipation is quite small, and $\mathbf{F}^{\mathrm{II}}$ is the EFM flux [3] derived from the collisionless Boltzmann equation. From the fact that the BGK model produces the Navier–Stokes terms by the first order perturbation from an equilibrium state, and Eq. (9b), we can see that the last flux $\mathbf{F}^{\mathrm{III}}$

accounts for the physical viscosity and heat conduction effects in case of viscous flows. Thus the flux $\mathbf{F}^{\mathrm{III}}$ is not essential in inviscid flows. The role of the spatial slopes as the physical dissipation in case of simple advection equations can be seen more clearly in Refs. [12, 13, 15]. From Eq. (26), it can be noted that in smooth region of the flow field where the collision time is small compared to the computational time step Δt, the influence of the flux $\mathbf{F}^{\mathrm{I}}$ becomes dominant due to the increase of $(1-\tau(1-e^{-\Delta t/\tau})/\Delta t)$. On the other hand, the role of the flux $\mathbf{F}^{\mathrm{EFM}}$ becomes significant near shock discontinuities because the increase of the collision time makes $\tau(1-e^{-\Delta t/\tau})/\Delta t$ large. For inviscid flows where the collision time is theoretically zero, $\mathbf{F}_{i+1/2,j}$ of Eq. (26) should become $\mathbf{F}^{\mathrm{I}}$. The flux $\mathbf{F}^{\mathrm{I}}$ alone, however, has difficulties in treating strong shock waves and expansion region as pointed out by Macrossan and Oliver [8] and Xu [9]. Thus the collision time has a non-zero small value even in smooth region and increases at shock discontinuities as in Eq. (25). The adjustment of the collision time according to flow characteristics couples the two flux terms, $\mathbf{F}^{\mathrm{I}}$ and $\mathbf{F}^{\mathrm{EFM}}$ suitably. This coupling mechanism is ascribed to the particle collision effect through the BGK model, which provides advantages over $\mathbf{F}^{\mathrm{I}}$ or $\mathbf{F}^{\mathrm{EFM}}$ alone in the computation of inviscid flows.

In viscous calculations, numerical dissipation from the convective fluxes, i.e., $\mathbf{F}^{\mathrm{I}}$ and $\mathbf{F}^{\mathrm{EFM}}$, should satisfy the constraint that it does not influence the physical dissipation. As will be shown in Section 3, however, a direct application of Eq. (26) to viscous calculations shows a noticeable deviation from experimental data and the results of other schemes due to the excessive numerical dissipation of $\mathbf{F}^{\mathrm{EFM}}$. As presented in the following section, this problem can be overcome not by changing the coupling mechanism built in the BGK numerical flux but by improving the flux component $\mathbf{F}^{\mathrm{EFM}}$ suitable for viscous flows.

2.2. *Gas-Kinetic Numerical Schemes for the Navier–Stokes Equations*

In computing inviscid flows where computational mesh is not highly stretched and a boundary layer does not need to be resolved, the coupling mechanism between the flux $\mathbf{F}^{\mathrm{I}}$ and $\mathbf{F}^{\mathrm{EFM}}$ provides adequate numerical dissipation to capture the inviscid flow physics. Some difficulties, however, may arise in viscous calculations against our anticipation that the flux $\mathbf{F}^{\mathrm{EFM}}$ would be influential only near shock discontinuities. Wherever the computational time step is small enough to be a similar order of the collision time, such as in the boundary layer with highly stretched cells, a close examination of Eq. (26) reveals that the portion of the flux $\mathbf{F}^{\mathrm{EFM}}$ is still large even in smooth flow region, hindering the flux $\mathbf{F}_{i+1/2,j}$ from capturing the contact discontinuity exactly and hence computing viscous flows. The excessive numerical dissipation from the flux $\mathbf{F}^{\mathrm{EFM}}$ directly influences the sensitive physical dissipation. The flux $\mathbf{F}^{\mathrm{I}}$ alone should be good enough to resolve a boundary layer but it cannot treat complex flows involving the interaction between shock waves (or expansion fans) and boundary layers. In order to overcome such difficulties, we consider the following two approaches.

Scheme 1. Following the approach taken by Moschetta and Pullin's EFMO scheme [10], we try to improve the flux $\mathbf{F}^{\mathrm{EFM}}$ by considering the Osher's linear subpath solution as

$$\mathbf{F}^{\mathrm{EFM}}_{\mathrm{mod}} = \mathbf{F}^{\mathrm{EFMO}} = \mathbf{F}^{+}_{l} + \mathbf{F}^{-}_{r} + \begin{cases} -\mathbf{F}^{-}(\mathbf{Q}_2) + \mathbf{F}^{-}(\mathbf{Q}_1), & u > 0 \\ \mathbf{F}^{+}(\mathbf{Q}_2) - \mathbf{F}^{+}(\mathbf{Q}_1), & u < 0, \end{cases} \tag{30}$$

where u denotes a common value of the normal velocity component at a cell interface and the subscripts 1 and 2 indicate intermediate states in Osher's scheme. We shall refer to the resulting scheme, i.e., $\mathbf{F}^{\mathrm{EFMO}}$ together with the fluxes $\mathbf{F}^{\mathrm{I}}$ and $\mathbf{F}^{\mathrm{III}}$, as Scheme 1. $\mathbf{F}^{\mathrm{EFMO}}$ flux

enables us to resolve the contact discontinuity exactly without deteriorating its shock capturing capability. However, it needs extra computational time compared to the flux $\mathbf{F}^{\mathrm{EFM}}$ and turns out to have some problems in resolving thermal boundary layer near a wall. This will be shown in the calculation of velocity and temperature profiles on a flat plate in Section 3. In addition, it turns out that this form of flux shows the transverse shock instability usually observed in Godunov-type schemes [2]. Thus we suggest Scheme 2 to remedy the problems.

Scheme 2. It is clearly seen from the mass flux of $\mathbf{F}^{\mathrm{EFM}}$ that when convection velocity is very small, as around a stagnation point or near a wall, the mass flux does not vanish and its numerical dissipation amounts to $(\rho_r a_r - \rho_l a_l)/2\alpha\sqrt{\pi}$, which is larger than that of van Leer's flux vector splitting scheme. In order to cure the problem by making the flux vanish near a wall, we modify the $\mathbf{F}^{\mathrm{EFM}}$ to have the form

$$\mathbf{F}^{\mathrm{EFM}}_{\mathrm{mod}} = \begin{pmatrix} M_l^+ a_{1/2}\rho_l \\ M_l^+ a_{1/2}\rho_l U_l + P_l^+ \rho_l/(2\lambda_l) \\ M_l^+ a_{1/2}\rho_l V_l \\ M_l^+ a_{1/2}\rho_l H_l \end{pmatrix} + \begin{pmatrix} M_r^- a_{1/2} pw(\rho_l, \rho_r) \\ M_r^- a_{1/2} pw(\rho_l U_l, \rho_r U_r) + P_r^- \rho_r/(2\lambda_r) \\ M_r^- a_{1/2} pw(\rho_l V_l, \rho_r V_r) \\ M_r^- a_{1/2} H_l\, pw(\rho_l, \rho_r) \end{pmatrix}$$

$$\text{if } (M_l^+ + M_r^-) > 0,$$

or

$$\begin{pmatrix} M_l^+ a_{1/2} pw(\rho_r, \rho_l) \\ M_l^+ a_{1/2} pw(\rho_r U_r, \rho_l U_l) + P_l^+ \rho_l/(2\lambda_l) \\ M_l^+ a_{1/2} pw(\rho_r V_r, \rho_l V_l) \\ M_l^+ a_{1/2} H_r\, pw(\rho_r, \rho_l) \end{pmatrix} + \begin{pmatrix} M_r^- a_{1/2}\rho_r \\ M_r^- a_{1/2}\rho_r U_r + P_r^- \rho_r/(2\lambda_r) \\ M_r^- a_{1/2}\rho_r V_r \\ M_r^- a_{1/2}\rho_r H_r \end{pmatrix}$$

$$\text{if } (M_l^+ + M_r^-) < 0,$$

with

$$pw(x, y) = (1 - w)x + wy, \qquad w = 1 - \min\left(\frac{p_l}{p_r}, \frac{p_r}{p_l}\right)^3. \tag{31}$$

Here, the common speed of sound $a_{1/2}$ is given by the simple arithmetic average of $(a_l + a_r)/2$. Both M_l and M_r, necessary for evaluating $M^{\pm}$ in Eq. (31), are redefined as $M_l = u_l/a_{1/2}$ and $M_r = u_r/a_{1/2}$. The modification of $\mathbf{F}^{\mathrm{EFM}}$ by introducing a common speed of sound $a_{1/2}$ at the cell interface is equivalent to the reflection of particle collisions at macroscopic level. Note that by ignoring the two terms $\rho_l a_l \exp(-\alpha^2 M_l^2)/8\alpha\lambda_l\sqrt{\pi}$ and $\rho_r a_r \exp(-\alpha^2 M_r^2)/8\alpha\lambda_r\sqrt{\pi}$ of Eq. (28) in Eq. (31), the flux $\mathbf{F}^{\mathrm{EFM}}_{\mathrm{mod}}$ together with the flux $\mathbf{F}^I$ conserves the total enthalpy. The pressure-based weighting function $pw(x, y)$ [26] introduced to prevent the postshock overshootings usually shown in AUSM+ scheme [18] is adopted here. In order to see the effect of the weighting function, the behavior of the mass flux of $\mathbf{F}^{\mathrm{EFM}}_{\mathrm{mod}}$ is examined. When $(M_l^+ + M_r^-) > 0$, the mass flux becomes

$$\mathbf{F}^{\mathrm{EFM}}_{1\mathrm{mod}} = M_l^+ a_{1/2}\rho_l + M_r^- a_{1/2} pw(\rho_l, \rho_r). \tag{32}$$

In smooth region where p_l and p_r are nearly the same, the weighting function pw becomes

ρ_l. Thus the mass flux takes the following form:

$$\mathbf{F}^{\mathrm{EFM}}_{1\mathrm{mod}} = M_l^+ a_{1/2}\rho_l + M_r^- a_{1/2}\rho_l = (M_l^+ + M_r^-)a_{1/2}\rho_l. \tag{33}$$

However, in the shock region where $p_l \ll p_r$, for example, the weighting function gives a value near ρ_r. Thus the mass flux becomes quite similar to that of the original EFM as

$$\mathbf{F}^{\mathrm{EFM}}_{1\mathrm{mod}} = M_l^+ a_{1/2}\rho_l + M_r^- a_{1/2}\rho_r, \tag{34}$$

where both properties before and after the shock are taken into account. The present modified flux $\mathbf{F}^{\mathrm{EFM}}_{\mathrm{mod}}$ seems to be similar, in smooth regions, to the AUSM+ scheme but one of its spurious behaviors, i.e., small oscillations adjacent to a wall, does not appear, owing to the fact that the flux $\mathbf{F}^{\mathrm{I}}$ still acts near a wall. We shall refer to $\mathbf{F}^{\mathrm{EFM}}_{\mathrm{mod}}$ along with $\mathbf{F}^{\mathrm{I}}$ and $\mathbf{F}^{\mathrm{III}}$ as Scheme 2. In addition, we assume the coefficient of $\mathbf{F}^{\mathrm{III}}$ in Eq. (29) to be $-\tau$ under the hydrodynamic limit, i.e., $\tau \ll \Delta t$ for both Scheme 1 and Scheme 2.

Prandtl Number Correction Method. Modification to the flux $\mathbf{F}^{\mathrm{III}}$ is needed in order to make the present scheme work for arbitrary Pr number, since the Chapman–Enskog expansion of the BGK relaxation model inherently gives $\mathrm{Pr} = 1$ [19]. A Prandtl number correction can be made by observing that the part yielding viscous diffusion and heat conduction effects is the $O(\tau)$ term in the BGK model [15]. From Eq. (19), $\tau(u\bar{a} + v\bar{b})g_0$ accounts for viscous and heat conduction fluxes, which are equivalent to $\mathbf{F}^{\mathrm{III}}$ in Eq. (26). Thus viscous stresses in the x- and y-directions and the energy diffusion correspond to $\mathbf{F}^{\mathrm{III}}_2 = \int u(u\bar{a} + v\bar{b})g_0\Psi_2\, d\Xi$, $\mathbf{F}^{\mathrm{III}}_3 = \int u(u\bar{a} + v\bar{b})g_0\Psi_3\, d\Xi$, and $\mathbf{F}^{\mathrm{III}}_4 = \int u(u\bar{a} + v\bar{b})g_0\Psi_4\, d\Xi$, respectively. Thus the correct heat conduction would be

$$-\nabla\cdot\mathbf{q} = \frac{1}{\mathrm{Pr}}\left(\mathbf{F}^{\mathrm{III}}_4 - U_0\mathbf{F}^{\mathrm{III}}_2 - V_0\mathbf{F}^{\mathrm{III}}_3\right). \tag{35}$$

This leads to the following modified energy flux as

$$\mathbf{F}^{\mathrm{III}}_{4\mathrm{mod}} = \frac{1}{\mathrm{Pr}}\mathbf{F}^{\mathrm{III}}_4 + \left(1 - \frac{1}{\mathrm{Pr}}\right)\left(U_0\mathbf{F}^{\mathrm{III}}_2 + V_0\mathbf{F}^{\mathrm{III}}_3\right), \tag{36}$$

where the subscript n denotes the nth component of the corresponding vector. The extra computational time for the present Pr number correction is nearly negligible because the moments required for Eq. (36) are already obtained during the calculation of the flux $\mathbf{F}^{\mathrm{III}}$.

2.3. *Efficient Time Integration Methods for Steady Flows*

As seen from Eq. (26), the present numerical flux is not only a function of flow variables at both sides of the cell interface but that of the collision time and computational time step, which might handicap the convergence to a steady state. Direct application of local time stepping to Eq. (26) leads to physically wrong solutions because of the imbalance of fluxes throughout a cell. In order to overcome this problem by deriving a time-independent flux, Xu *et al.* [13] ignored all the slope terms in the distribution functions f_0 and g as

$$f_0 = \begin{cases} g^l, & x < 0 \\ g^r, & x > 0 \end{cases}, \tag{37a}$$

$$g = g_0. \tag{37b}$$

Substituting Eqs. (37a), (37b) into Eq. (6), the solution of f at the cell interface is

$$f = g_0 + e^{-t/\tau}(f_0 - g_0), \tag{38}$$

where $e^{-t/\tau}$ was replaced by a small parameter ε which was designed empirically to become large near shock discontinuities. The numerical flux from these distribution functions with Runge–Kutta time stepping and multigrid method was applied to inviscid airfoil calculations. However, the viscous flux from the Navier–Stokes equations should be added explicitly for viscous calculations, since this method disregards the spatial slope terms in the distribution function g. Also, the effect of the numerical dissipation in Eq. (38) on the physical dissipation has to be resolved.

The present time integration, while keeping the spatial slope terms in Eq. (9b) to simulate viscous effects, is performed as (for the sake of brevity formulation in one-dimensional case is given)

$$\mathbf{Q}_i^{n+1} = \mathbf{Q}_i^n - \frac{\Delta t}{\Delta x}\left\{\mathbf{F}_{i+1/2}(\mathbf{Q}_{i+1}, \mathbf{Q}_i, \tau, \Delta t) - \mathbf{F}_{i-1/2}(\mathbf{Q}_i, \mathbf{Q}_{i-1}, \tau, \Delta t)\right\}, \tag{39}$$

where $\mathbf{F}$ is the numerical flux in the x-direction. In order to implement local time stepping, Eq. (39) is changed into

$$\mathbf{Q}_i^{n+1} = \mathbf{Q}_i^n - \frac{\Delta t_l}{\Delta x}\left\{\mathbf{F}_{i+1/2}(\mathbf{Q}_{i+1}, \mathbf{Q}_i, \tau, \Delta t_n) - \mathbf{F}_{i-1/2}(\mathbf{Q}_i, \mathbf{Q}_{i-1}, \tau, \Delta t_n)\right\}, \tag{40}$$

where Δt_n is a flux averaging time step and Δt_l is a local time step satisfying the CFL condition as

$$\Delta t_l = \mathrm{CFL}\frac{\Delta x}{|u| + a}. \tag{41}$$

This form of the time integration guarantees the flux balance throughout a cell. The flux averaging time step Δt_n used for all steady calculations in this paper is given by

$$\Delta t_n = \frac{\min(\Delta t_l)}{2\mathrm{CFL}}, \tag{42}$$

where $\min(\Delta t_l)$ takes the minimum value among the local time step Δt_l s. The reason for this specific averaging is that this will make solution accuracy equal to that of the Euler forward time integration by the minimum time step with $\mathrm{CFL} = 0.5$. In viscous calculations, a time step restriction due to diffusion effects is also taken into account in Eq. (41) as in Ref. [20].

For the time integration of steady state problems, Euler backward implicit integration is thought to be preferable to multi-stage Runge–Kutta method, since the method evaluates residuals only once per iteration and allows a larger time step. Applying Newton type linearization to the present flux,

$$\mathbf{F}^{n+1} = \mathbf{F}(\mathbf{Q}^{n+1}) = \mathbf{F}^n + \Delta\mathbf{F} + O(\Delta t^2) = \mathbf{F}^n + \left(\frac{\partial \mathbf{F}}{\partial \mathbf{Q}}\right)(\mathbf{Q}^{n+1} - \mathbf{Q}^n) + O(\Delta t^2), \tag{43}$$

where the flux averaging time step in the numerical flux is assumed to be constant. A standard Δ-form with the above linearization is expressed by

$$\left(\mathbf{I}/\Delta t_l + \frac{\partial}{\partial x}\left(\frac{\partial \mathbf{F}_x}{\partial \mathbf{Q}}\right)\right)\Delta Q = -\mathbf{R}, \tag{44}$$

where $\mathbf{I}$ is an identity matrix and $\mathbf{R}$ denotes a residual vector, or the summation of all fluxes throughout a cell. In evaluating the flux Jacobian $\partial\mathbf{F}/\partial\mathbf{Q}$ in Eq. (44), only the contribution of $\mathbf{F}^{\mathrm{EFM}}$ out of the total numerical flux $\mathbf{F}_{i+1/2,j}$ is considered to reduce the computing time. After this approximate linearization, flux Jacobians are discretized in an upwind manner as

$$\left(\mathbf{I}/\Delta t_l + \frac{1}{\Delta x}(\delta_x^- \mathbf{A}^+ + \delta_x^+ \mathbf{A}^-)\right)\Delta Q = -\mathbf{R} \tag{45}$$

with

$$\mathbf{A}^+ = \frac{\partial \mathbf{F}_l^+}{\partial \mathbf{Q}_l} = \frac{\partial}{\partial Q_l}\int_0^\infty u g_l \Psi \, d\Xi, \qquad \mathbf{A}^- = \frac{\partial \mathbf{F}_r^+}{\partial \mathbf{Q}_r} = \frac{\partial}{\partial \mathbf{Q}_r}\int_{-\infty}^0 u g_r \Psi \, d\Xi,$$

where $\delta_x^\pm$ denote the forward and backward difference in the x-direction. In the two-dimensional case, the left hand side is efficiently inverted by the ADI (Alternating Direction Implicit) method. In an effort to reduce the computational cost of the evaluation of the present flux Jacobian, the Jacobian from van Leer's flux [17] was tested regardless of the flux on the right hand side of Eq. (45). However, it only gave about one-third of the stable time step of the present flux Jacobian in a few airfoil test cases.

In order to accelerate the convergence to a steady state, a multigrid procedure is implemented into the present implicit time integration. We follow the multigrid procedure in Ref. [21]. Denoting a mesh level by subscript, the flow variables of the fine mesh are restricted to the coarse mesh by area weighting as

$$\mathbf{Q}_{2h}^{(0)} = \sum S_h \mathbf{Q}_h / S_{2h}, \tag{46}$$

where S_h is the cell area of the fine mesh and S_{2h} is the sum of the area over four cells in the fine mesh. Then the solutions on the coarse mesh are updated as follows.

(1) Calculate corrections, and update solutions on the fine mesh.

(2) Restrict the flow variables to the coarse mesh.

(3) Collect the residual over the four cells of the fine mesh, and calculate a forcing function to get the residual on the coarse mesh as

$$\mathbf{R}_{2h}^* = \mathbf{R}_{2h}(\mathbf{Q}_{2h}) + \sum \mathbf{R}_h(\mathbf{Q}_h) - \mathbf{R}_{2h}\left(\mathbf{Q}_{2h}^{(0)}\right). \tag{47}$$

(4) Calculate corrections and update solutions on the coarse mesh. The residual for the next coarser mesh is calculated similarly as

$$\mathbf{R}_{4h}^* = \mathbf{R}_{4h}(\mathbf{Q}_{4h}) + \sum \mathbf{R}_{2h}^* - \mathbf{R}_{4h}\left(\mathbf{Q}_{4h}^{(0)}\right). \tag{48}$$

The procedure is repeated down to the coarsest mesh and finally sends corrections back to the fine mesh by bilinear interpolation. One of the important requirements for an efficient multigrid procedure is that the time integration method should effectively damp out high frequency errors. Since we do not optimize the time integration of Eq. (45) to serve this purpose, more research may be needed here for a better convergence characteristics. Nevertheless, there is quite an improvement over a single grid calculation in steady state problems, as will be shown in numerous tests in the following section. In this paper, the V-cycle is adopted for all calculations.

3. NUMERICAL RESULTS

In this section, we demonstrate the capability of the present schemes with carefully selected test cases ranging from one-dimensional shock tube problems to viscous turbulent flows around airfoils with a two-equation turbulence model. In one-dimensional calculations, the spatial slope term for the y-direction in Eq. (9b) is, of course, not considered. The computational time is advanced with the Euler forward method for unsteady problems. Since there is no noticeable difference between Scheme 1 and Scheme 2 in terms of solution accuracy and convergence characteristics except for the thermal boundary layer and transverse shock instability test problems, we apply Scheme 2 in most of the test cases. For inviscid calculations, Scheme 2 is used in order to show that the present modification works consistently for inviscid flow fields as well as for viscous flows.

Case 1. Various one-dimensional shock tube problems are solved here to confirm the accuracy and robustness of Scheme 2, and results are compared with those of Roe's FDS scheme. The result of the classical Sod test with 100 cells is shown in Fig. 1. A shock wave and a contact discontinuity are captured with the comparable accuracy of Roe's scheme, and both corners of the rarefraction wave are resolved more sharply with the current method.

The next test case is quite similar to the previous one, but with special initial conditions given as $\rho_l = 3,\ u_l = 0.9,\ p_l = 3$ and $\rho_r = 1,\ u_r = 0.9,\ p_r = 1$, a sonic point exists along a rarefraction wave. Thus, Roe's scheme without an entropy fix shows an entropy-violating solution. The present method, however, prevents the formation of an expansion shock as in Fig. 2 confirming that the present scheme satisfies the entropy condition.

The results of complicated interactions from two blast waves with 400 cells are shown in Fig. 3. It is also evident in this test case that noticeable difference is not observed between the present and Roe's scheme with regard to solution accuracy.

With the introduction of the pressure-based weighting function in Eq. (31), a postshock overshooting is much suppressed, as shown in a head-on shock collision test case with the

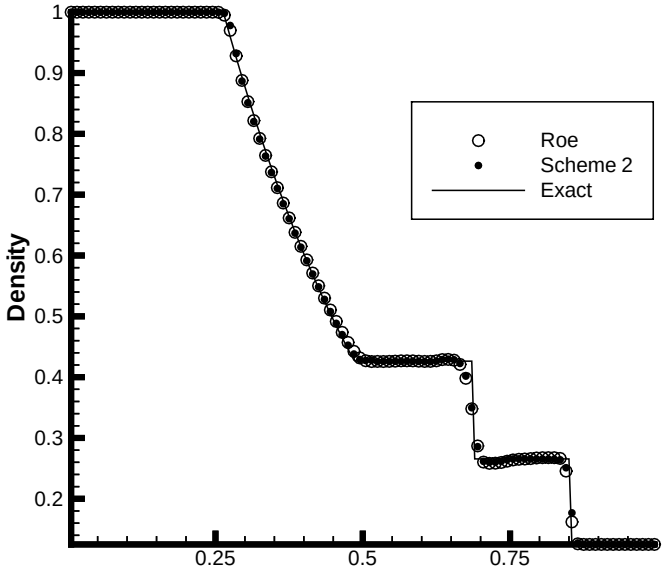

FIG. 1. Sod test case.

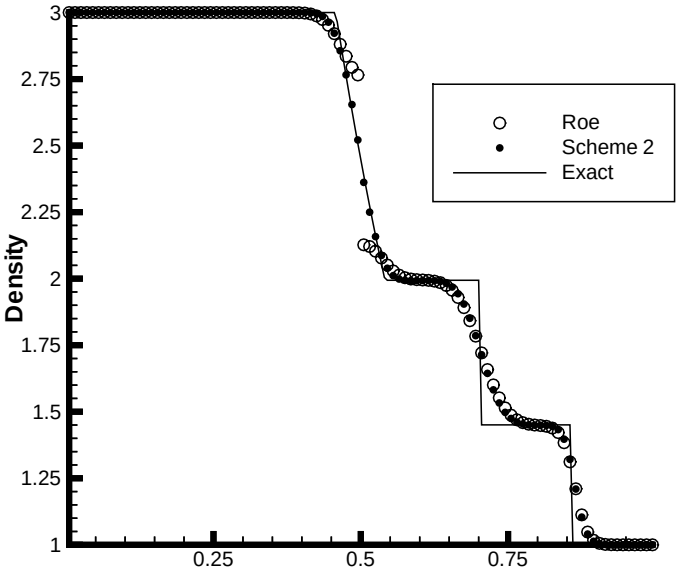

FIG. 2. Sod test case with a sonic point in expansion waves.

initial conditions of $M_l = -M_r = 25$ in Fig. 4. The temperature glitch at the symmetry line is observed like other classical upwind schemes, but weaker than that of Roe' scheme.

A supersonic expansion test [22] with the initial conditions of $\rho_l = 1$, $u_l = -2$, $\varepsilon_l = 3$ and $\rho_r = 1$, $u_r = 2$, $\varepsilon_r = 3$ is solved to see whether or not Scheme 2 preserves the positivity of density and energy. Many Godunov-type schemes including Roe's scheme may fail in this test problem, of which cure generally lies in the modification of wave speeds at the expense

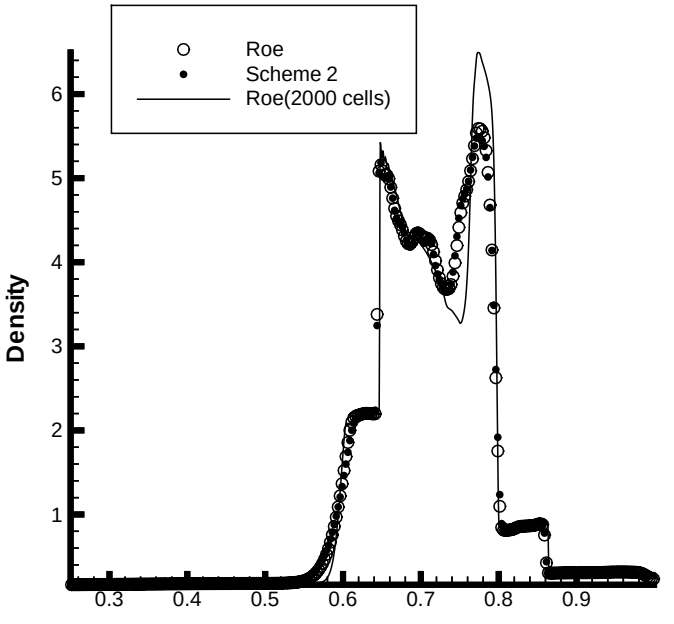

FIG. 3. Woodward–Collela blasting wave test case.

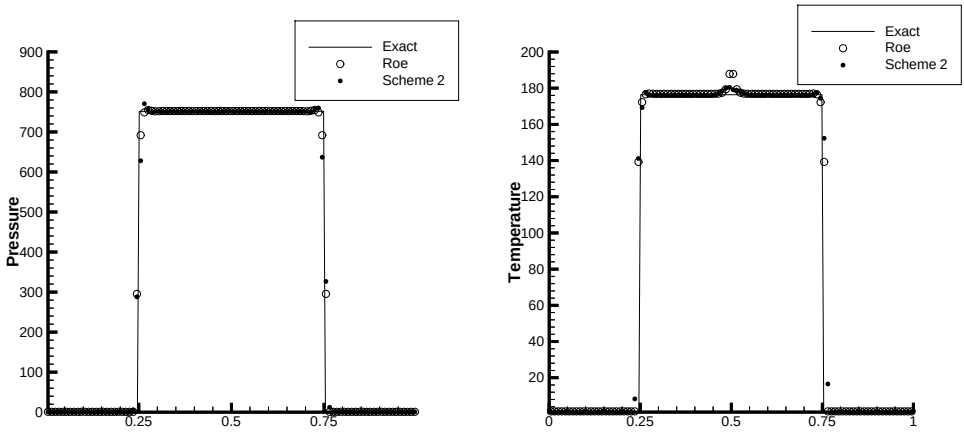

FIG. 4. Colliding flows with $M_l = -M_r = 25$.

of accuracy. But Scheme 2 faces no difficulty in near vacuum flows as shown in Fig. 5, and Scheme 1 also survives this test case.

Case 2. Inviscid steady state transonic flow calculations for the RAE2822 and NACA0012 airfoils are presented with Scheme 2. The implicit time integration method with the local time stepping and four-level multigrid developed in Section 2.3 is applied on an O-type mesh with 160 circumferential and 32 radial cells. A typical O-type mesh is shown in Fig. 6. The Cp distribution of the RAE2822 airfoil at $M = 0.75$, $\alpha = 3^\circ$, and the L_2 norm error of density are shown in Fig. 7. Advantages of the present scheme over the EFM scheme based on the collisionless Boltzmann equation can be seen. The present scheme captures a shock within one interior cell, while the EFM within two or three cells. The multigrid method relieves computational burden significantly, considering the overhead of four-level multigrid is about 50% of the single grid computation. The error history of the Euler forward time integration in Eq. (39) without any convergence acceleration method is shown for comparison. Figure 8 shows the Cp distribution and error history of the NACA0012 airfoil at $M = 0.8$, $\alpha = 1.25^\circ$. A shock is captured in two interior cells and the computational time is effectively reduced by the multigrid method. Next, we demonstrate the accuracy sensitivity with respect to the variation of the coefficient C_2 in Eq. (25). Figure 9 shows

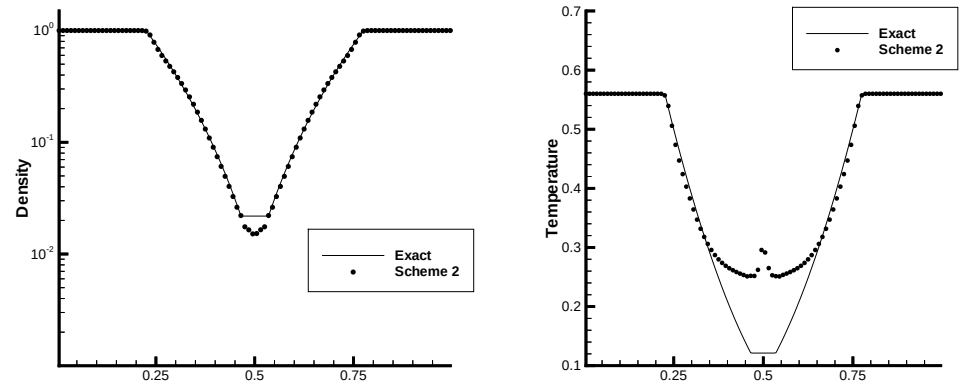

FIG. 5. Supersonic expansion test case with $\rho_l = 1$, $u_l = -2$, $\varepsilon_l = 3$ and $\rho_r = 1$, $u_r = 2$, $\varepsilon_r = 3$.

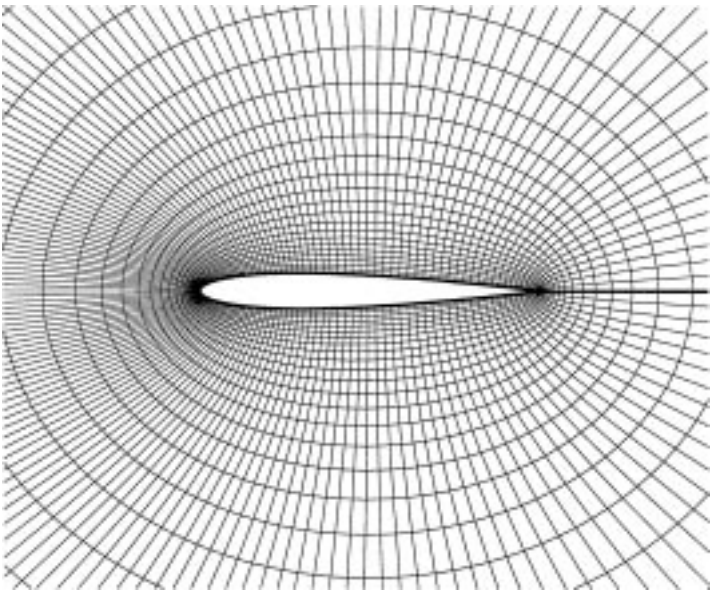

FIG. 6. Typical O-type mesh around an airfoil.

Cp distributions with $C_2 = 0.0001$, 0.01, and 1.0, from which we can confirm that although C_2 varies by four orders of magnitude, the shock is captured within one or two cells. As expected from the form of the collision time in Eq. (25), Cp distributions nearly match each other in the smooth region. All these results reveal that the present method captures shock waves within one or two interior cells, and provides a good accuracy and efficiency for transonic flows.

Case 3. This test case is taken from the paper by Quirk [2]. A strong shock wave propagates on the long two-dimensional duct mesh with perturbed center lines. Figure 10 shows the Mach number contours of Roe's FDS, Scheme 1, and Scheme 2 with $C_2 = 0.01$. After 5000 iterations, Roe's FDS shows the so-called carbuncle in which the shock structure

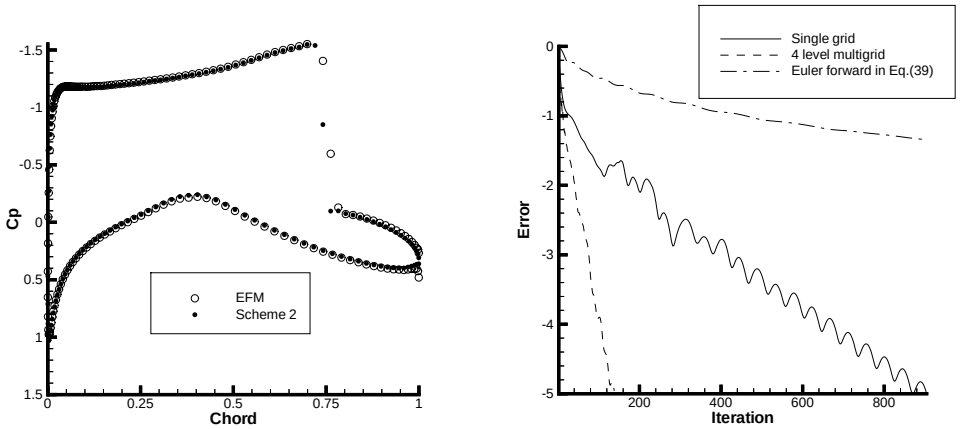

FIG. 7. Cp distribution and error history of RAE2822 airfoil at $M = 0.75$, $\alpha = 3^\circ$ with $C_L = 1.0973$, $C_D = 0.0463$.

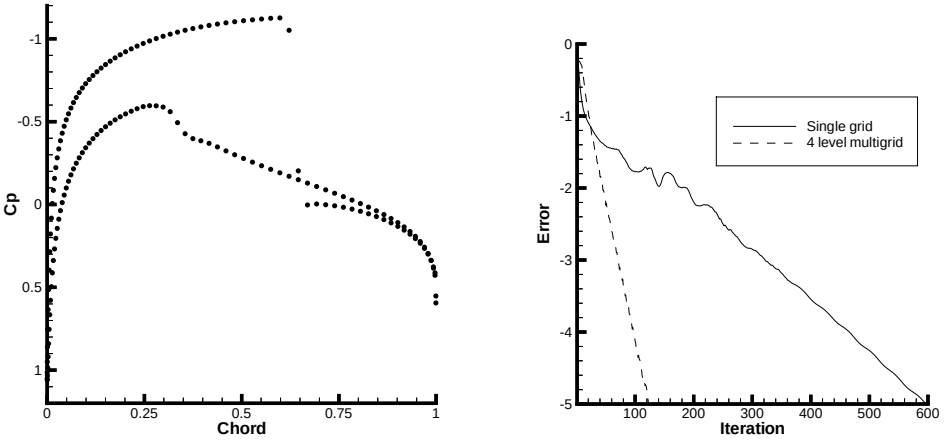

FIG. 8. Cp distribution and error history of NACA0012 airfoil at $M = 0.8$, $\alpha = 1.25^\circ$ with $C_L = 0.3538$, $C_D = 0.0229$ (Scheme 2).

is completely destroyed. Scheme 2 cleanly captures the shock. According to the linearized analysis by Gressier *et al.* [27], the EIM scheme (or equivalently the TTT scheme) is marginally stable with regard to the disturbance. In the current test case, perturbations do not seem to grow with time due to the influence of the flux $\mathbf{F}^{\mathrm{EFM}}_{\mathrm{mod}}$ near the shock. Symptom of transverse shock instability may be induced with a smaller value of C_2 due to the dominance of the flux $\mathbf{F}^{\mathrm{I}}$, but not as severely as Roe's scheme. On the other hand, Scheme 1 also exhibits the carbuncle phenomenon as Roe's scheme owing to its resemblance with Godunov-type schemes.

Case 4. It is well known that Godunov-type schemes show a kinked Mach stem in the double Mach reflection problem. Gressier *et al.* [27] have shown that even the AUSM+ scheme on a refined mesh can suffer from the kinked Mach stem, too. The test is set up by 30° ramp and a moving shock at $M_s = 5.5$. In Fig. 11, the density contours of Scheme 2 with $C_2 = 0.01$, the AUSM+ scheme, and the AUSM+ scheme with the pressure-based weighting function as in Eq. (31) are shown on a 400×400 mesh. The results are obtained with the first order spatial accuracy. The kink is about to develop in the AUSM+ scheme at the

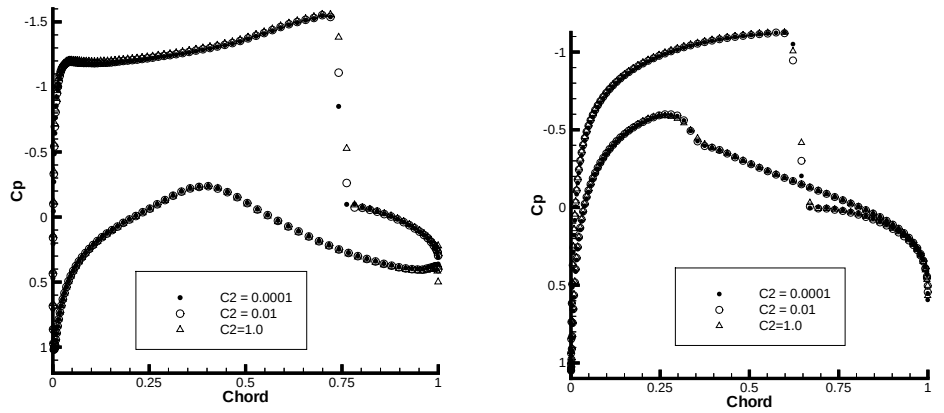

FIG. 9. Sensitivity of Cp distribution according to the variation of C_2 (Scheme 2).

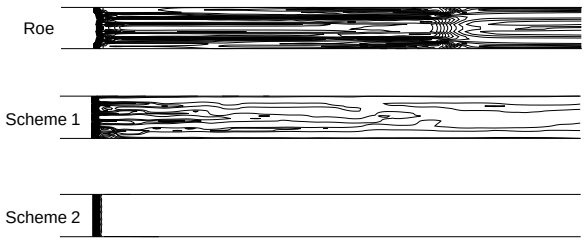

FIG. 10. Mach number contours of even–odd perturbed grid problem with 100 contour levels.

principal Mach stem while the present scheme and AUSM+ scheme with the pressure-based weighting function do not show such behavior. Inferring from these results, the pressure-based weighting function in Eq. (31) seems to prevent or, at least, delay the formation of the kinked Mach stem.

Case 5. A boundary layer on a flat plate at $M = 0.2$ and $\mathrm{Re} = 10^4$ is calculated. A rectangular mesh system with 81×33 cells is generated to maintain nearly the same number of points in the boundary layer along the plate. In Fig. 12, non-dimensionalized x and y velocity profiles are shown at $x/L = 0.3, 0.6, 0.8$, and compared with the Blasius profiles. A good agreement and convergence acceleration are achieved with Scheme 1 and Scheme 2. However, the numerical flux of Eq. (26) without modifications to the flux $\mathbf{F}^{\mathrm{EFM}}$ cannot accurately predict the boundary layer for the reasons discussed in Section 2.2. Also, the boundary layer calculation carried out with the flux from g only as in Ref. [13] is believed to be difficult to compute viscous flows with shock waves. On the other hand, both Scheme 1 and Scheme 2 are able to capture shock waves as well as contact discontinuities important for viscous calculations. With the same free stream conditions and mesh distribution, a thermal boundary layer with adiabatic wall boundary condition at various Pr numbers is calculated. The Pr number correction is implemented into Scheme 1 and Scheme 2. As shown in Fig. 13, the temperature distribution with Scheme 1 is overpredicted near a wall, contrary to the authors' argument [10] that the physical viscosity would damp out the temperature glitch near the wall in viscous flows. The reason is not yet clearly explained, but refined mesh close to the wall mitigates the discrepancy. Scheme 2, however, shows good agreements with exact solutions at various Pr numbers.

Case 6. This test case is two-dimensional laminar flows characterized by an oblique shock with an incident angle of 32.6° upon a flat plate causing a boundary layer to separate and reattach around the shock impinging region. The complicated phenomenon provides a good test of validating a scheme before a turbulence model is implemented. Computational

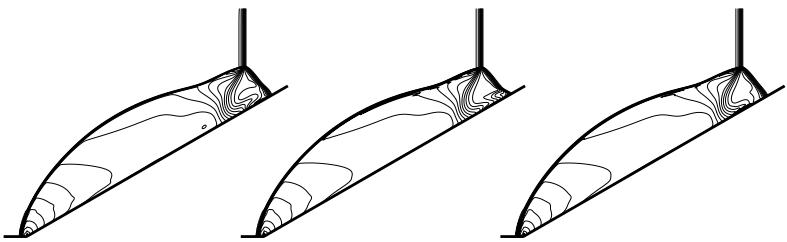

FIG. 11. Density contours of double Mach reflection on 400×400 mesh (left: Scheme 2, center: AUSM+, right: AUSM+ with pressure-based weighting function in Eq. (31)).

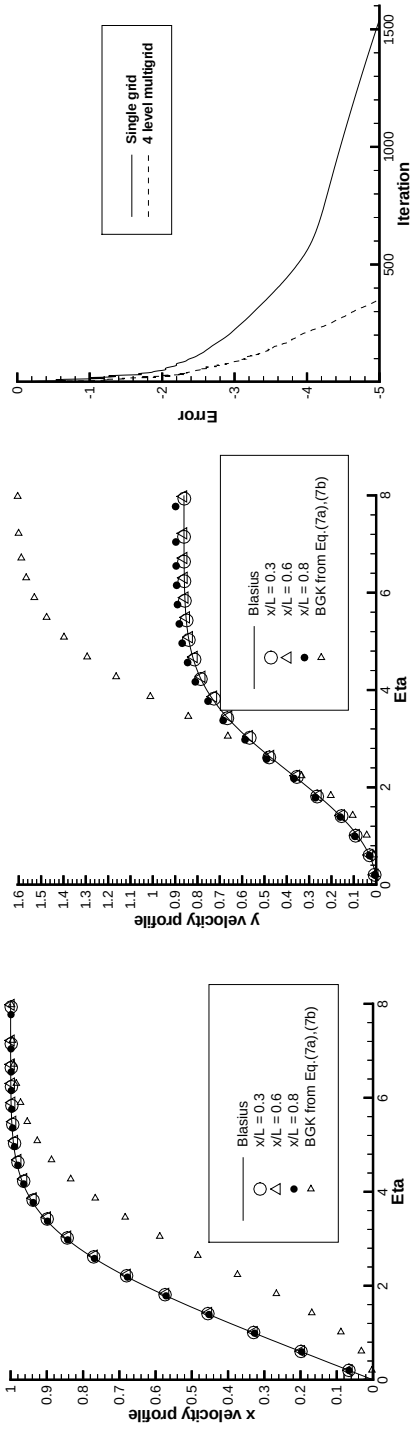

FIG. 12. Boundary layer calculation on a flat plate at $M = 0.2$, $\mathrm{Re} = 10^4$ with 16 cells in boundary layer (Scheme 2 and the BGK scheme from Eqs. (7a), (7b)).

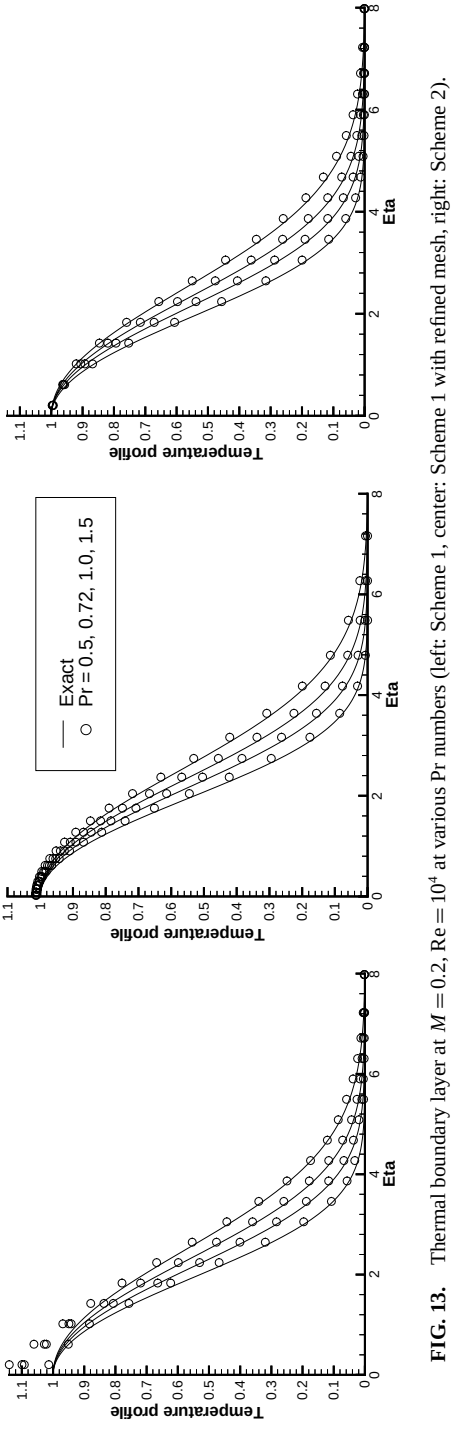

FIG. 13. Thermal boundary layer at $M = 0.2$, $\mathrm{Re} = 10^4$ at various Pr numbers (left: Scheme 1, center: Scheme 1 with refined mesh, right: Scheme 2).

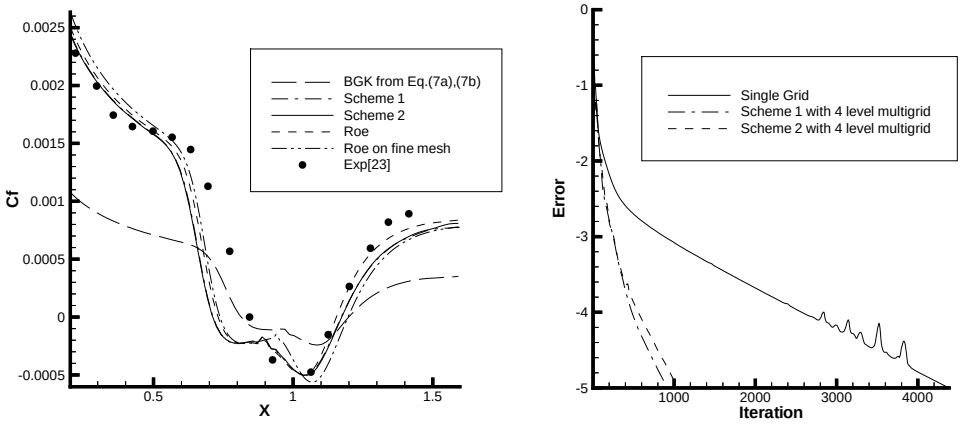

FIG. 14. Skin friction coefficient and error history of shock–boundary layer interaction problem at $M = 2.0$, $\mathrm{Re} = 2.96 \times 10^5$.

results are obtained at $M = 2.0$, $\mathrm{Re} = 2.96 \times 10^5$ on 105×65 mesh and compared with the experimental results of Degrez [23]. In Fig. 14, skin friction coefficients from Scheme 1 and Scheme 2 are compared with the results of Roe's scheme on the same mesh and on the finer mesh of 257×129 cells, indicating that the overall accuracy of the present schemes is quite acceptable. It also shows that the current schemes are adequate for viscous flows, while the original BGK scheme yields a large deviation from other results. A careful examination of pressure contours in Fig. 15 reveals that Scheme 2 captures the shock more

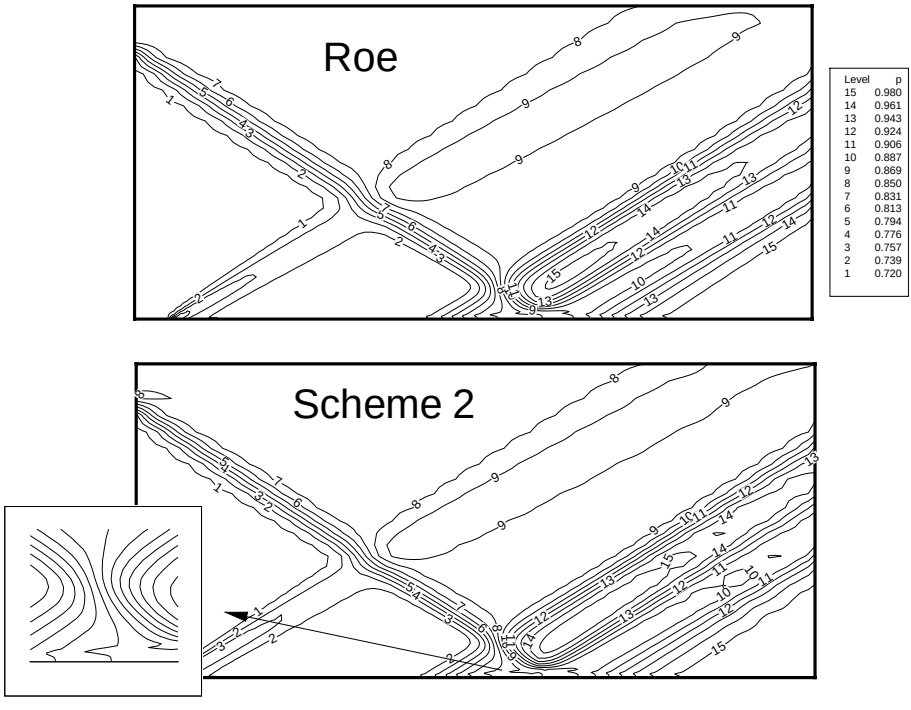

FIG. 15. Pressure contours of shock–boundary layer interaction.

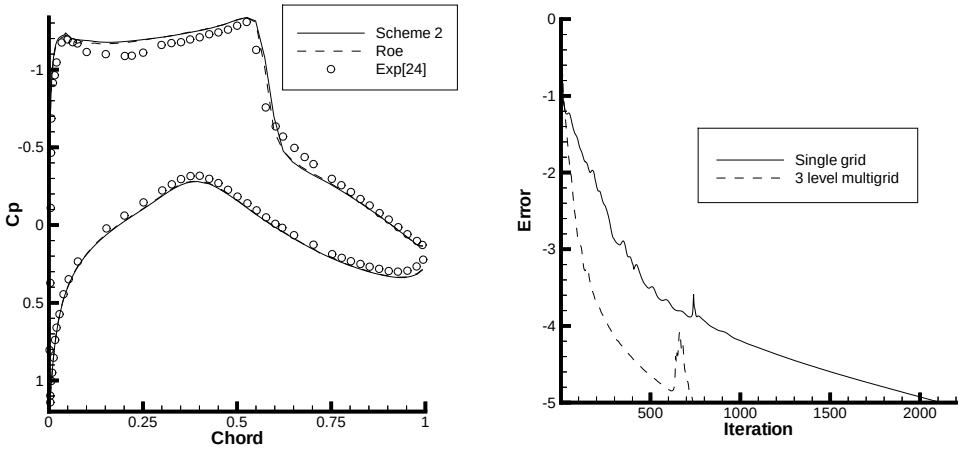

FIG. 16. Cp distribution and error history at $M = 0.73, \alpha = 2.79^\circ$ and $\mathrm{Re} = 6.5 \times 10^6$ with the Baldwin–Lomax turbulence model, $C_L = 0.8714$, $C_D = 0.0195$.

sharply than Roe's scheme, and does not exhibit spurious oscillations near a wall that can be observed in AUSM+ scheme. An efficient reduction of the computational cost is achieved through multigrid technique, as shown in Fig. 14. As mentioned earlier, there seems to be no noticeable difference between Scheme 1 and Scheme 2 in terms of solution accuracy and convergence characteristics.

Case 7. The last test case is concerned with viscous turbulent flows around the RAE2822 airfoil at transonic regime. In order to incorporate turbulence effect into the current schemes,

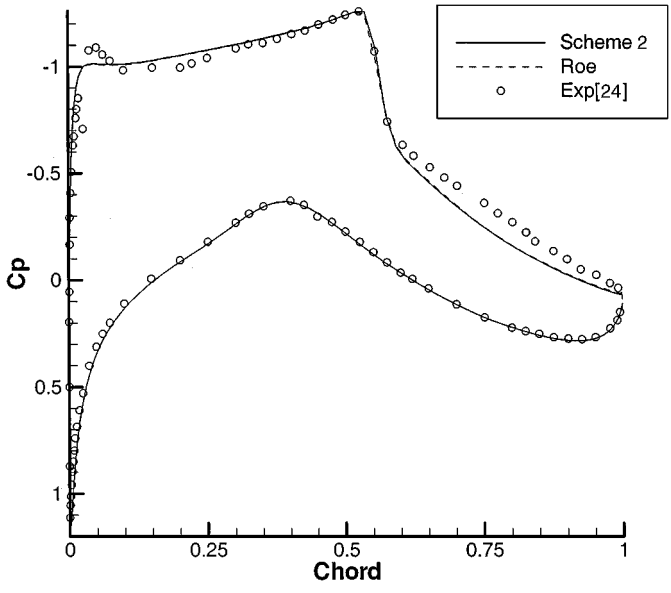

FIG. 17. Cp distribution of RAE2822 airfoil at $M = 0.75$, $\alpha = 2.79^\circ$ and $\mathrm{Re} = 6.2 \times 10^6$ with the $k - \omega$ SST model, $C_L = 0.7641$, $C_D = 0.0253$.

TABLE I
Computational Cost of Proposed Schemes

Roe's FDS + viscous flux	Original BGK scheme from Eqs. (7a), (7b) *without* $\bar{A}$	Scheme 1	Scheme 2
1	1.29	1.84	1.33

the collision time in Eq. (24) is changed accordingly as

$$\hat{\tau} = \frac{M_\infty(\hat{\mu} + \hat{\mu}_t)}{\mathrm{Re}_\infty \hat{p}} + C_2 \frac{\sqrt{\hat{\lambda}_0}}{\hat{\rho}_0} |\hat{p}^l - \hat{p}^r|, \tag{49}$$

where $\hat{\mu}_t$ is the eddy viscosity obtained from an appropriate turbulence model depending on the physical situation of flow fields. Figure 16 shows Cp distribution and error history on 241×48 C-type mesh at $M = 0.73$, $\alpha = 2.79^\circ$, and $\mathrm{Re} = 6.5 \times 10^6$ corresponding to the experimental Case 9 in Ref. [24]. The Baldwin–Lomax turbulence model is used. Differences between Scheme 2 and Roe's scheme are hardly noticeable. For the Case 10 where the Baldwin–Lomax turbulence model usually fails to predict the correct shock position, the two equation $k - \omega$ SST turbulence model by Menter [25] is adopted. Figure 17 shows a fairly accurate Cp distribution compared with the experimental results. Free stream conditions for the computation are $M = 0.75$, $\alpha = 2.79^\circ$ and $\mathrm{Re} = 6.2 \times 10^6$. In both calculations, the flow is assumed to be fully turbulent without any transition near the leading edge. As can be seen from the computed results, the present scheme works well with any turbulence model.

Finally, the computational efficiency of the proposed schemes is presented. Due to many moments calculations including error functions, the flux component $\mathbf{F}^{\mathrm{III}}$ takes a relatively large computing time. In order for a fair comparison, however, the current schemes are compared with other ones for viscous calculations. Table I shows the relative computational cost of several schemes for the Navier–Stokes computations with the second order spatial accuracy and one-step explicit time integration. Note that, unlike the original BGK scheme by Xu [11], the temporal slope $\bar{A}$ is not included in the present comparison, which reduces the computational time substantially. If $\bar{A}$ is included, the required computing time is noticeably larger than that of Scheme 2. The computational costs of Scheme 1 and Scheme 2 are more expensive than Roe's FDS scheme with viscous flux. Considering the various desirable properties especially for Scheme 2, however, the computational burden is compensated. We believe that there is still a room for a speed-up of the present schemes if a faster algorithm for the evaluation of error functions is used. In the present paper, the routine in SPECFUN package available at `www.netlib.org` is used, which applies the Chebyshev approximation.

4. CONCLUDING REMARKS

From the Boltzmann equation with the BGK approximation, an improved gas-kinetic BGK scheme suitable for compressible inviscid and viscous flows is developed. The original BGK numerical flux for viscous flows is turned out to be a non-linear coupling among Pullin's EFM [3], EIM by Macrossan and Oliver [8] (or equivalently TTT by Xu [9]) and

viscous flux, where the coupling mechanism is governed by the BGK model. In order to guarantee the accurate resolution of viscous and thermal boundary layer involving shock waves, one component of the BGK numerical flux, i.e., the EFM flux, is modified, and an efficient method for the Prandtl number correction is developed. For efficient steady state calculations, convergence acceleration methods such as local time stepping and multigrid techniques consistent with the present implicit formulation are developed.

Although there is still a room to improve the computational efficiency and optimal formulation of the collision time of the proposed schemes, numerous computational tests performed in this paper show that the present schemes are able to solve a wide range of aerodynamic problems accurately without sacrificing the robustness of the original BGK scheme. Especially, Scheme 2, keeping a high level of accuracy comparable to Godunov-type schemes, is considered to possess many desirable properties that cannot be found in other well known schemes.

APPENDIX

The form of the flux $\mathbf{F}^{\mathrm{III}}$ in Eq. (29) with the Prandtl number correction of Eq. (36) is explicitly presented. Before writing out the flux, the formula for the evaluation of the Maxwellian distribution with the limits of $(-\infty, \infty)$ is given. After the definition for the moments of the Maxwellian g_0 with respect to q is introduced as

$$\langle q \rangle = \int q \frac{g_0}{\rho} \, d\Xi, \tag{50}$$

the moments of ξ appearing in the evaluation of distribution functions are given by

$$\langle \xi^2 \rangle = \frac{K}{2\lambda_0}, \quad \langle \xi^4 \rangle = \frac{K(K+2)}{4\lambda_0^2} \tag{51}$$

and

$$\begin{aligned} \langle u^0 \rangle &= 1, \ \langle u^1 \rangle = U_0, \\ \langle u^{n+2} \rangle &= U_0 \langle u^{n+1} \rangle + \frac{n+1}{2\lambda_0} \langle u^n \rangle. \end{aligned} \tag{52}$$

The same formula can be applied to the moment of the Maxwellian distribution function with respect to v by replacing U_0 with V_0 in Eq. (52), and

$$\langle u^l v^m \xi^n \rangle = \langle u^l \rangle \langle v^m \rangle \langle \xi^n \rangle. \tag{53}$$

Then, the flux $\mathbf{F}^{\mathrm{III}}$ can be expressed as

$$\begin{aligned} \mathbf{F}_1^{\mathrm{III}} = \int u(u\bar{a} + v\bar{b}) g_0 \, d\Xi &= \rho_0 \big(a_1 \langle u^2 \rangle + a_2 \langle u^3 \rangle + a_3 \langle u^2 v \rangle + a_4 \langle u^4 + u^2 v^2 + u^2 \xi^2 \rangle \\ &+ b_1 \langle uv \rangle + b_2 \langle u^2 v \rangle + b_3 \langle u v^2 \rangle + b_4 \langle u^3 v + u v^3 + u v \xi^2 \rangle \big), \end{aligned} \tag{53a}$$

$$\begin{aligned} \mathbf{F}_2^{\mathrm{III}} = \int u(u\bar{a} + v\bar{b}) u g_0 \, d\Xi &= \rho_0 \big(a_1 \langle u^3 \rangle + a_2 \langle u^4 \rangle + a_3 \langle u^3 v \rangle + a_4 \langle u^5 + u^3 v^2 + u^3 \xi^2 \rangle \\ &+ b_1 \langle u^2 v \rangle + b_2 \langle u^3 v \rangle + b_3 \langle u^2 v^2 \rangle + b_4 \langle u^4 v + u^2 v^3 + u^2 v \xi^2 \rangle \big), \end{aligned} \tag{53b}$$

$$\mathbf{F}_3^{\mathrm{III}} = \int u(u\bar{a} + v\bar{b})v g_0 \, d\Xi = \rho_0\big(a_1\langle u^2 v\rangle + a_2\langle u^3 v\rangle + a_3\langle u^2 v^2\rangle + a_4\langle u^4 v + u^2 v^3 + u^2 v\xi^2\rangle + b_1\langle u v^2\rangle + b_2\langle u^2 v^2\rangle + b_3\langle u v^3\rangle + b_4\langle u^3 v^2 + u v^4 + u v^2 \xi^2\rangle\big), \tag{53c}$$

$$\mathbf{F}_4^{\mathrm{III}} = \int u(u\bar{a} + v\bar{b})\frac{1}{2}(u^2 + v^2 + \xi^2) g_0 \, d\Xi = \frac{1}{2}\rho_0\big(a_1\langle u^4 + u^2 v^2 + u^2\xi^2\rangle + a_2\langle u^5 + u^3 v^2 + u^3\xi^2\rangle + a_3\langle u^4 v + u^2 v^3 + u^2 v\xi^2\rangle + a_4\langle u^6 + u^2(v^4 + \xi^4) + 2u^4 v^2 + 2\xi^2(u^4 + u^2 v^2)\rangle + b_1\langle u^3 v + u v^3 + u v\xi^2\rangle + b_2\langle u^4 v + u^2 v^3 + u^2 v\xi^2\rangle + b_3\langle u^3 v^2 + u v^4 + u^3 v^2\xi^2\rangle + b_4\langle u^5 v + u v(v^4 + \xi^4) + 2u^3 v^3 + 2v\xi^2(u^4 + u^2 v^2)\rangle\big). \tag{53d}$$

In actual coding, Eqs. (53a)–(53d) can be efficiently implemented since the moments such as $\langle u^{0-3}\rangle$, $\langle v^{0-2}\rangle$, and $\langle \xi^2\rangle$ are already obtained during the calculation of the flux $\mathbf{F}^{\mathrm{I}}$ in Eq. (27), and there are many common factors. Applying the Prandtl number correction, the corrected $\mathbf{F}_4^{\mathrm{III}}$ can be expressed as

$$\mathbf{F}_{4\,\mathrm{mod}}^{\mathrm{III}} = \mathbf{F}_4^{\mathrm{III}}/\mathrm{Pr} + \big(\langle u\rangle \mathbf{F}_2^{\mathrm{III}} + \langle v\rangle \mathbf{F}_3^{\mathrm{III}}\big)(1 - 1/\mathrm{Pr}). \tag{54}$$

ACKNOWLEDGMENTS

The authors appreciate financial support by the Korea Science and Engineering Foundation (Grant 98-0200-14-01-3) and by the Korea Research Foundation (Grant 98-1020-30-3) for the present work. We also thank the referees for their careful and rigorous comments on the manuscript.

REFERENCES

1. P. L. Roe, Approximate Riemann solver, parameter vectors, and difference schemes, *J. Comput. Phys.* **43**, 357 (1981).
2. J. J. Quirk, A contribution to the great Riemann solver debate, *Int. J. Numer. Meth. Fluids* **18**, 555 (1994).
3. D. I. Pullin, Direct simulation methods for compressible inviscid ideal-gas flow, *J. Comput. Phys.* **34**, 231 (1980).
4. R. D. Reitz, One-dimensional compressible gas dynamics calculations using the Boltzmann equation, *J. Comput. Phys.* **42**, 108 (1981).
5. B. Perthame, Second-order Boltzmann schemes for compressible Euler equations in one and two space dimensions, *SIAM J. Numer. Anal.* **29**, 1 (1992).
6. J. C. Mandal and S. M. Deshpande, Kinetic flux vector splitting for Euler equations, *Comput. Fluids* **23**, 447 (1994).
7. A. Harten, P. D. Lax, and B. van Leer, On upstream differencing and Godunov-type schemes for hyperbolic conservation laws, *SIAM Rev.* **25**, 35 (1983).
8. M. N. Macrossan and R. I. Oliver, A kinetic theory solution method for Navier–Stokes equations, *Int. J. Numer. Meth. Fluids* **17**, 177 (1993).
9. K. Xu, Numerical hydrodynamics from gas-kinetic theory, Ph.D. thesis, Columbia University (1993).
10. J-M. Moschetta and D. I. Pullin, A robust low diffusive kinetic scheme for the Navier–Stokes/Euler equations, *J. Comput. Phys.* **133**, 193 (1997).
11. K. Xu and K. H. Prendergast, Numerical hydrodynamics from gas-kinetic theory, *J. Comput. Phys.* **109**, 53 (1993).

12. K. Xu and K. H. Prendergast, Numerical Navier–Stokes solutions from gas kinetic theory, *J. Comput. Phys.* **114**, 9 (1994).
13. K. Xu, L. Martinelli, and A. Jameson, Gas-kinetic finite volume methods, flux-vector splitting, and artificial diffusions, *J. Comput. Phys.* **120**, 48 (1995).
14. P. L. Bhatnagar, E. P. Gross, and M. Krook, A model for collision processes in gases. I. Small amplitude processes in charged and neutral one-component systems, *Phys. Rev.* **94**, 511 (1954).
15. C. Kim and A. Jameson, A robust and accurate LED-BGK solver on unstructured adaptive meshes, *J .Comput. Phys.* **143**, 598 (1998).
16. B. van Leer, Towards the ultimate conservative difference scheme. V. A second order sequel to Godunov's method, *J. Comput. Phys.* **23**, 101 (1979).
17. B. van Leer, Flux-vector splitting for the Euler equations, *Lecture Notes Phys.* **170**, 507 (1982).
18. M. S. Liou, Progress towards an Improved CFD Method: AUSM+, AIAA Paper 95-1701-CP (1995).
19. W. G. Vincenti and C. H. Kruger, *Introduction to Physical Gas Dynamics* (Wiley, New York, 1965).
20. L. Martinelli, Calculation of Viscous Flows with a Multigrid Method, Ph.D. thesis (Princeton University, 1987).
21. A. Jameson and S. Yoon, Lower-upper implicit schemes with multiple grids for the Euler equations, *AIAA J.* **24**, 1737 (1986).
22. B. Einfeldt, C. D. Munz, P. L. Roe, and B. Sjögreen, On Godunov-type methods near low densities, *J. Comput. Phys.* **92**, 273 (1991).
23. G. Degrez, C. H. Boccadoro, and J. F. W. Wendt, The interaction of an oblique shock wave with a laminar boundary layer revisited. An experimental and numerical study, *J. Fluid Mech.* **177**, 246 (1987).
24. P. H. Cook, M. A. McDonald, and M. C. P. Firmin, *AEROFOIL RAE 2822 Pressure Distributions, Boundary Layer and Wake Measurements*, AGARD Advisory Report 138 (1979).
25. F. R. Menter, Two-equation eddy-viscosity turbulence models for engineering applications, *AIAA J.* **32**, 1598 (1994).
26. K. H. Kim, J. H. Lee, and O. H. Rho, An improvement of AUSM schemes by introducing the pressure-based weight functions, *Comput. Fluids* **27**, 311 (1998).
27. J. Gressier and J-M. Moschetta, On the Pathological Behavior of Upwind Schemes, AIAA Paper 98-0110 (1998).